^{15}N Relaxation Studies of Apo-Mts1: A Dynamic S100 Protein[†]

Kaushik Dutta,*[,‡] Cathleen J. Cox,[§,||] Ravi Basavappa,[§,⊥] and Steven M. Pascal*[,#]

New York Structural Biology Center, 89 Convent Avenue, New York, New York 10033, Department of Biochemistry and Biophysics, University of Rochester Medical Center, Box 712, Rochester, New York 14642, and Institute of Fundamental Science, Massey University, Palmerston North, New Zealand

Received March 24, 2008; Revised Manuscript Received May 14, 2008

ABSTRACT: Mts1 is a member of the S100 family of EF-hand calcium-binding proteins. Like most S100 proteins, Mts1 exists as a dimer in solution and contains one canonical and one pseudo-EF-hand motif per monomer, each of which consists of two α helices connected by a loop capable of coordinating a calcium ion. The backbone dynamics of murine apo-Mts1 homodimer have been examined by nuclear magnetic resonance spectroscopy. Longitudinal and transverse relaxation data and steady-state ^{1}H−^{15}N nuclear Overhauser effects were analyzed using model-free formalism. The extracted global correlation time is 9.94 ns. Results indicate that the protein backbone is most rigid at the dimer interface, made up of helices 1 and 4 from each monomer with mean S^2 (S^2_{avg}) values ∼0.9, flanked by helices 2 and 3 with lower S^2_{avg} values of 0.84 and 0.77, respectively. Each calcium-binding site along with the hinge joining the two EF-hands and the N- and C-termini are considerably more flexible than the dimer interface on a range of time scales and more flexible than the corresponding regions of other S100 proteins studied to date. As the hinge and the C-terminal tail are believed to interact with target proteins, these dynamic characteristics may have implications for Mts1 activity.

Mts1, also known as S100A4, is a small (∼24 kDa dimer), highly soluble protein belonging to the S100 family of EF-hand-containing calcium-binding proteins. Numerous lines of evidence implicate Mts1 in tumor metastasis. The expression level of Mts1 in various cell lines correlates with metastatic potential (*1*). Introduction of Mts1 into nonmetastatic cell lines confers the metastatic phenotype (*2*). Reducing available Mts1 mRNA through ribozyme techniques reduces the metastatic character of tumor cells (*3*). Mating transgenic mice carrying the mts1 gene with mice susceptible to tumors of low metastatic potential produces offspring with increased tumor aggressiveness (*4*). Mts1 expression occurs in tissue and cell types normally capable of motility, such as activated macrophages, T-lymphocytes, trophoblast cells, and embryonic tissue, suggesting that the role of Mts1 in metastasis is linked to cellular motility (*5*). Consistent with this hypothesis, nonmuscle myosin II has been identified as a cellular binding partner for Mts1 (*5*). In the presence of calcium, Mts1 binds to the C-terminal end of the myosin heavy chain, close to the regulatory phosphorylation site, inhibiting casein kinase 2-mediated phosphorylation and self-assembly of nonmuscle myosin (*6*). Thus, the mechanism of Mts1-induced cell motility may involve reorganization of cytoskeletal components (*5*).

Another target for Mts1 is the p53 tumor suppressor (*7*). Mts1 binds to the C-terminal regulatory domain of p53 and inhibits phosphorylation of p53 by protein kinase C. This interaction interferes with the DNA-binding activity of p53 and plays a functional role in modulating p53 target gene transcription. In this way, Mts1 may cooperate with p53 in apoptosis induction and cell cycle regulation. Mts1 is also shown to interact with an endothelial plasminogen coreceptor called annexin II. Upon this interaction, plasminogen activation in endothelial cells is accelerated. There is some evidence that Mts1 can also interact with a distinct group of target proteins in a calcium-independent manner (*8*).

Most S100 family members are EF-hand-containing calcium-binding proteins. An EF-hand motif typically consists of a loop region flanked by two α helices. To coordinate calcium, the canonical EF-hand motif makes use of six residues from a highly acidic 12-residue stretch centered about the loop region, with calcium interactions mediated primarily via side chain oxygens. Members of the S100 family generally contain one canonical EF-hand (C-terminal) and a variant form of EF-hand (N-terminal). The variant or "pseudo"-EF-hand coordinates calcium using principally backbone carbonyl oxygens from six residues over a highly basic 14 amino acid stretch.

The S100 family of proteins share significant amino acid sequence similarity. Regions of greatest sequence variation occur in the C-terminal tail and in the hinge between helices 2 and 3. The hinge from many S100 proteins, including S100B, S100A1, and calbindin D_{9k}, has been shown to have little regular secondary structure and in several cases is

[†] NIH P41 GM66354 and NYSTAR support NMR resources at NYSBC. Support for R.B. included a Research Scholarship of the Leukemia and Lymphoma Society of America.

* To whom correspondence should be addressed. K.D.: voice, 212-939-0660ext 9304; fax, 212-939-0863; e-mail, dutta@nysbc.org. S.M.P.: voice, +646 356 9099ext 3558; fax, +646 350 5682; e-mail, s.pascal@massey.ac.nz.

[‡] New York Structural Biology Center.

[§] University of Rochester Medical Center.

[||] Present address: Department of Physics, St. John Fisher College, 3690 East Ave., Rochester, NY 14618.

[⊥] Present address: Program Director, National Institute of General Medical Sciences, National Institutes of Health, Bethesda, MD 20892.

[#] Massey University.

10.1021/bi8005048 CCC: $40.75
Published on Web 07/15/2008

known to be involved in interactions with protein targets. For example, the binding interface between S100B and p53 involves the hinge, helix 3, and helix 4 (*9*), and the binding interfaces of both S100A11 with annexin I (*10*) and S100A10 with annexin II (*11*) involve residues in the hinge, helix 1, and helix 4. In most cases, binding to target proteins is calcium-dependent. Calcium binding can confer a dramatic reorientation of helix 3 and the hinge, exposing a large hydrophobic region on the surface of the protein which is critical for the interaction of S100 proteins with their effector molecules. For example, in both S100B (*12*) and S100A6 (*13*), helix 3 reorients by ~90° relative to helix 4 upon the addition of calcium. In the case of S100B, this reorientation exposes 18 of the 21 residues involved in the p53 interaction (*9*).

Unlike other EF-hand proteins, S100 family members typically form noncovalent homodimers with 2-fold symmetry. The only known exception is calbindin D_{9k} (*14*). Structural studies of S100 proteins indicate that each monomer forms a unicornate four-helix bundle. The dimerization interface is formed by antiparallel alignment of helices 1, 1′, 4, and 4′ (the primes indicate helices from the partner molecule) which form a characteristic X-type four-helix bundle. In addition, several S100 family members are capable of heterodimerization, including S100A8 with S100A9 (*15*), S100B with S100A1 (*16*), and Mts1 with S100A1 (*6*).

Protein dynamics over a wide range of time scales and amplitudes plays an important role in biological functions such as enzyme reaction, ligand binding, and folding (*17*–*19*). NMR spectroscopy provides unique opportunities to explore a wide range of dynamic time scales such as fast internal motion (ps−ns), slow motion (μs−ms), the overall correlation time of a protein (of the order of 10 ns), and even very slow conformational exchange motions (ms−days), with site-specific resolution. S100 family proteins share a common three-dimensional structure yet bind to distinctive ligands. This selectivity is in general thought to involve the highly variable hinge and/or the C-terminal tail regions. These regions have been shown to be affected by binding of calcium to two less variable regions of the protein; e.g., see ref *20*. Regions of proteins which coordinate calcium or contact ligands can undergo large conformational changes upon coordination which are often foreshadowed by the ability of the same regions of the protein to undergo large conformational changes in the absence of the ligand; e.g., see ref *21*. If these motions occur on a ms−μs time scale, as large changes often do, they can in many cases be detected as an exchange contribution to relaxation (R_{ex}). In order to begin to understand the role conformational flexibility in Mts1 may play in specific activation of the metastatic pathway, we have undertaken an examination of apo-Mts1 relaxation rates and internal dynamics. This work includes an assessment of fast internal motions and slower, conformational exchange in the Mts1 backbone. We report that the protein backbone is most rigid at the dimer interface and more flexible in the N-terminal half of each calcium-binding site, the hinge region, and the C-terminal tail. Comparison of these results with relaxation studies of other members of the S100 family reveals some similarity in regions of conserved secondary structure but significantly more flexibility in regions correlating with specific protein activity.

MATERIALS AND METHODS

Sample Preparation. Recombinant mouse Mts1 was expressed and purified as described previously (*20*). Briefly, *Escherichia coli* strain BL21(DE3) CodonPlus was transformed with the plasmid H-MBP-3C (*22*) containing the murine mts1 gene. The final protein product contains the full 101 amino acids of murine Mts1 plus an additional 5 N-terminal residues (GPGSA). ^{15}N-labeled protein was produced by cell growth in M9 minimal media using $^{15}NH_4Cl$ as the sole nitrogen source. Cells were purified by batch method using cobalt affinity resin, followed by anion-exchange column chromatography. The sample was exchanged into buffer containing 5 mM Tris-HCl and 1 mM EDTA, pH 6.0, and concentrated to 1.1 mM. Sodium azide was added to 50 μM, and D_2O was added to 5% v/v.

Measured Relaxation Parameters. All NMR experiments were performed at 40 °C. A complete set of T_1, T_2, and $^1H-^{15}N$ NOE measurements were made at 600 MHz using a Varian Unity 600 MHz spectrometer equipped with three rf channels and *z*-axis field gradients. An additional set of T_2 measurements were recorded at 500 MHz on a Varian Inova spectrometer with three rf channels and *z*-axis field gradients. Relaxation rate constants were obtained from peak intensities in $^1H-^{15}N$-correlation spectra acquired with variable transverse (10, 30 (×2), 50, 70, 90, 110, 130, 150, 170, 190, 210 ms) and longitudinal (10, 30 (×2), 50, 90, 130, 230, 350, 470, 950, and 1200 ms) relaxation delays. Relaxation-compensated CPMG experiments (RC-CPMG) (*23*) were performed to determine the average R_2 ($R_2^{avg} = {}^1/_2(R_2 + R_{2I_xs_x})$ value with $\tau_{CP} = 1$ and 10 ms, where τ_{CP} is the delay between the 180° pulses of the CPMG cycle. The relaxation delays used were 0 (×2), 8, 16, 32, 48, 80 (×2), 112, and 160 ms for $\tau_{CP} = 1$ ms and 0 (×2), 40, 80, 120 (×2), 160, and 200 ms for $\tau_{CP} = 10$ ms. Recycle delays of 1.5 s were used in all cases.

To directly identify residues with significant chemical exchange contribution to transverse relaxation rates, we used the methodology proposed by Kroenke et al. (*24*), where the chemical exchange contribution to transverse relaxation is given by

$$R'_{ex} = R_2 - R_2^0 \quad (1)$$

where R_2 is measured by CPMG. The relaxation delays used to obtain the R_2 rates were 0 (×2), 16.9, 33.8, 67.6, 84.6, 101.5, 118.4, 135.3, and 169.1 ms. R_2^0, the transverse relaxation rate in the absence of R_{ex}, can be obtained by measuring η_{xy}, the cross-correlation rates between ^{15}N CSA and $^{15}N-^1H$ dipolar relaxation (*25*) and then using the equation $R_2^0 = \kappa\eta_{xy}$, where κ is independent of chemical exchange and local motions (*26*). The cross-correlation rates (η_{xy}) were measured using the symmetrical reconversion method developed by Pelupessy et al. (*27*), and κ was determined iteratively as an average of R_2^0/η_{xy} for all residues that were not subject to chemical exchange processes, assuming that the ^{15}N CSA is constant for all residues (*24*). The average value of κ at 600 MHz was found to be 1.61 and was also independently verified using an unrelated

[1] Abbreviations: EDTA, ethylenedinitrilotetraacetic acid; NOE, nuclear Overhauser effect; CSI, chemical shift indexing; MHC-II, myosin heavy chain II.

protein. The above set of experiments was carried out on a 600 MHz Bruker spectrometer equipped with cryoprobe.

All data were processed with nmrPipe and visualized with NMRdraw and NMRview (*28*). Peak intensity was measured with NMRview, and errors in intensities were estimated from duplicate spectra at one relaxation delay time. The relaxation rates R_1, R_2, and R_2^{avg} were determined by fitting the experimental data to a single exponential function given by $I(t) = I_0e^{-Rt}$, where $R = R_1$, R_2, or R_2^{avg} using the CURVEFIT program (A. G. Palmer III, Columbia University). The residues whose peaks in the spectra overlapped were not included in the analysis.

The steady-state $^{15}N-^{1}H$ NOE relaxation data sets were recorded using 48 scans per point and by recording two spectra with and without a 3.0 s period of proton saturation (*29*) following an initial 1.0 s recycle delay. The error (σ_{NOE}) was determined using the equation:

$$\sigma_{NOE} = \frac{I_{sat}}{I_{unsat}}\left(\left(\frac{\sigma_{sat}}{I_{sat}}\right)^2 + \left(\frac{\sigma_{unsat}}{I_{unsat}}\right)^2\right)^{1/2} \quad (2)$$

where I_{sat} and I_{unsat} represent the measured intensities of a particular resonance in the presence and absence of proton saturation and σ_{sat} and σ_{unsat} represent the root-mean-square variation in the noise in empty spectral regions of the spectra with and without proton saturation.

Lipari and Szabo Model-Free Analysis. Relaxation data were analyzed following the model-free formalism of Lipari and Szabo (*30*). This method uses two types of "model-free" parameters to describe motion: the generalized order parameter (S^2) that indicates the amplitude and the correlation time which models the time scale of an internal motion. In the formalism of Lipari and Szabo, the spectral density function is given by

$$J(\omega) = \frac{S^2\tau_c}{1+\omega^2\tau_c^2} + \frac{(1-S^2)\tau}{1-\omega^2\tau^2} \quad (3)$$

where τ_c is the global rotational correlation time and $\tau = \tau_c\tau_e/(\tau_c + \tau_e)$.

Clore et al. expanded this formalism to account for internal motion on two distinct time scales, which differ by at least one order of magnitude (*31*). An exchange term, R_{ex}, is also utilized to account for slower conformational exchange processes which affect transverse relaxation times. The spectral density function in this case (for isotropic tumbling) is

$$J(\omega) = \frac{S^2\tau_c}{1+\omega^2\tau_c^2} + \frac{(1-S_f^2)\tau'_f}{1+\omega^2\tau'_f} + \frac{(S_f^2-S^2)\tau'_s}{1+\omega^2\tau'_s} \quad (4)$$

Fast and slow order parameters (S_f^2 and S_s^2, where $S^2 = S_f^2S_s^2$) and two internal correlation times (τ_f and τ_s) are used. This equation reduces to eq 3 when $S_s^2 = 1$ and thus $S^2 = S_f^2$.

The ^{15}N T_1 and T_2 relaxation times and the $^{1}H-^{15}N$ NOE are related to the spectral density, $J(\omega)$, by

$$\frac{1}{T_2} = R_2 = \left(\frac{d^2}{8}\right)[4J(0) + J(\omega_H - \omega_N) + 3J(\omega_N) + 6J(\omega_H) + 6J(\omega_H + \omega_N)] + \left(\frac{c^2}{6}\right)[4J(0) + 3J(\omega_N)] \quad (5)$$

$$\frac{1}{T_1} = R_1 = \left(\frac{d^2}{4}\right)[J(\omega_H - \omega_N) + 3J(\omega_N) + 6J(\omega_H + \omega_N)] + c^2J(\omega_N) \quad (6)$$

$$NOE = 1 + \left(\frac{d^2}{4R_1}\right)\left(\frac{\gamma_N}{\gamma_H}\right)[6J(\omega_H + \omega_N) - J(\omega_H - \omega_N)] \quad (7)$$

where $d = \mu_o h\gamma_N\gamma_H\langle r_{NH}^{-3}\rangle/(8\pi^2)$ and $c = \omega_N\Delta\sigma/\sqrt{3}$ and μ_o is the permeability of free space, h is Planck's constant, γ_H and γ_N are the gyromagnetic ratios of the ^{1}H and ^{15}N spins, r_{NH} (1.02 Å) is the N−H bond length, ω_H and ω_N are the Larmor frequencies of the ^{1}H and ^{15}N spins, and $\Delta\sigma$ is the chemical shift anisotropy of the ^{15}N nucleus (−170 ppm) assuming an axially symmetric chemical shift tensor.

Rotational Diffusional Anisotropy. A preliminary value for the rotational correlation time (τ_c) was estimated from analysis of a subset of residues selected based on two criteria. First, residues with $^{1}H-^{15}N$ NOE less than 0.6 were omitted. Second, from this subset, residues with R_1 or R_2 values deviating significantly from average values were omitted, as described by the following acceptance criteria:

$$\frac{R_{2i} - \langle R_2\rangle}{\langle R_2\rangle} - \frac{R_{1i} - \langle R_1\rangle}{\langle R_1\rangle} < 1.5\sigma \quad (8)$$

where $\langle R_j\rangle$ and R_{ji} (j = 1, 2 and i = ith residue) are the average rates and R_1 and R_2 are the individual rates of the subset of remaining residues satisfying the first criteria. σ is the standard deviation of $\{(R_{2i} - \langle R_2\rangle)/\langle R_2\rangle\} - \{(R_{1i} - \langle R_1\rangle)/\langle R_1\rangle\}$. Based on these criteria, a total of 53 residues were used to estimate the overall correlation time and rotational diffusion tensors. An average solution structure of apo-Mts1 (pdb accession 1M31) was used for the estimation of the overall correlation time and rotational diffusion tensors. The F-test analysis was performed to choose between isotropic, axially symmetric, and fully anisotropic diffusion models. A probability factor (P%), which indicates the probability that improvement in fitting when model complexity increases is coincidental, was calculated for the isotropic−axially symmetric pair of models and for the fully anisotropic−axially symmetric pair of models. Probability factors >5% are not statistically significant.

Relaxation data (R_1, R_2 at 600 MHz and R_2 at 500 MHz) and steady-state $^{1}H-^{15}N$ NOE values at 600 MHz along with the N−H vector orientations obtained from the average solution structure of apo-Mts1 were used to obtain the model-free parameters via the program DYNAMICS (*32*). The relaxation data were fitted to six models using the following approximations for $J(\omega)$: Model 1 describes "very fast" internal motion:

$$J(\omega) = \frac{2}{5}\left(\frac{S_f^2\tau_c}{1+\omega^2\tau_c^2}\right) \quad (9)$$

with τ_f < 10 ps and $S_s^2 = 1$. S_f^2 is the sole internal motion parameter extracted. Model 2 describes "fast (but not very fast)" motion:

$$J(\omega) = \frac{2}{5}\left(\frac{S_f^2\tau_c}{1+\omega^2\tau_c^2}\right) + \frac{(1-S_f^2)\tau'_f}{1+\omega^2\tau'^2_f} \quad (10)$$

where $\tau'_f = \tau_c\tau_f/(\tau_c + \tau_f)$ with τ_f typically on the order of 100 ps and $S_s^2 = 1$. The first two models are similar except

that, in model 1, the second term in model 2 is negligible at pertinent frequencies, due to a "very small" value of τ_f. Survival of the second term in model 2 allows extraction of both S_f^2 and τ_f.

Model 5 allows for a combination of "very fast" and "slow" motion. Slow motion, which is considered negligible in all other models, can approach to within about an order of the global correlation time:

$$J(\omega) = \frac{2}{5}\left(\frac{S_f^2 S_s^2 \tau_c}{1+\omega^2\tau_c^2}\right) + \frac{S_f^2(1-S_s^2)\tau'_s}{1+\omega^2\tau'^2_s} \qquad (11)$$

where $\tau'_s = \tau_c\tau_s/(\tau_c + \tau_s)$. S_f^2, S_s^2, and τ_s are extracted. Models 3, 4, and 6 are identical to models 1, 2, and 5, respectively, but with an R_{ex} term added to the expression for R_2 to account for ms−μs time scale conformational exchange.

Model selection for each N−H bond vector was done according to the procedure given in Mandel et al. (*33*). The model-free parameters were optimized by minimizing χ^2, defined as (*32*)

$$\chi^2 = \sum_i \frac{(R_1^{ext} - R_1^{calc})^2}{\sigma_{R_{1i}}^2} + \frac{(R_2^{ext} - R_2^{calc})^2}{\sigma_{R_{2i}}^2} + \frac{(NOE^{ext} - NOE^{calc})^2}{\sigma_{NOEi}^2} \qquad (12)$$

where calc and ext represent the calculated and experimentally determined parameters, respectively, and σ_{R_1}, σ_{R_2}, and σ_{NOE} are experimentally determined uncertainties. If more than one of the spectral density functions satisfied these conditions, the model with the fewest parameters necessary to fit the data was selected.

After selecting the best model for each N−H bond vector, the global correlation time was reoptimized and model selection repeated utilizing the optimized τ_c value. This process was repeated until further iteration resulted in no further improvement in fitting.

Hydrodynamic model calculations were carried out using the program HYDRONMR (*34*) and compared with the experimental data. The R_2/R_1 ratio is not affected by rapid internal motions or by the magnitude of CSA (*35*) and therefore can be used for comparing experimental and calculated data, once residues with low frequency motion and/or conformation exchange are excluded from the calculation. The protocol for the estimation of the optimal atomic element radius (AER) is described elsewhere (*34*). Using the above criteria and the lowest energy NMR structure of apo-Mts1 (pdb accession 1M31), optimal AER was found to be 2.215 Å and was used to calculate the theoretical hydrodynamic parameters.

RESULTS AND DISCUSSION

Dynamics of Mts1. Complete sequential backbone resonance assignment has been reported elsewhere (*36*). Ten residues were omitted from relaxation analysis due to spectral overlap. Figure 1 shows the R_1, R_2, and $^1H-^{15}N$ NOE data and R_2/R_1 ratio at 600 MHz. R_2 values at 500 MHz are also shown. The average R_1 rate was 1.65 ± 0.37 s^{-1} (10% trimmed mean 1.62 s^{-1}) while the average R_2 rates at 600 and 500 MHz were 12.86 ± 3.1 s^{-1} (10% trimmed mean 12.9 s^{-1}) and 11.14 ± 2.73 s^{-1} (10% trimmed mean 11.23 s^{-1}), respectively. The average heteronuclear NOE was 0.55 ± 0.21 (10% trimmed mean 0.58). After eliminating residues with NOE <0.6 or with significant R_{ex} contributions to R_2, the remaining 53 amino acids were used to calculate hydrodynamic parameters. The initial estimate of the overall correlation time (τ_c) was 9.54 ns with an average tensor ratio ($D_\parallel/D_\perp$) of 1.14. Note that the axial tensor ratio obtained for a highly homologous S100B protein was 1.16 (*37*). The Mts1 global correlation time was also calculated independently of model-free analysis via HYDRONMR (*34*). This procedure yielded an almost identical τ_c value of 9.55 ns.

There was not significant improvement in the probability of fit upon increasing the complexity of the model from isotropic to axially symmetric. These initial estimates were used to fit the complete set of relaxation data (R_1, R_2, NOE at 600 MHz and R_2 at 500 MHz) using the model-free formalism approach (*30, 38*) to both isotropic and axially symmetric models. The final anisotropy of the diffusion tensor and the average correlation time were found to be 1.15 ($D_\parallel/D_\perp$) and 9.94 ns, respectively. It has been shown that, in the case of a molecule with 20% or less anisotropy, the choice of an isotropic vs axially symmetric model has a negligible effect on the hydrodynamic parameters (*39*). In addition, the hydrodynamic parameters (e.g., generalized order parameter) were very similar when the data were fitted to isotropic or axially symmetric models, with a correlation coefficient of 0.99. Therefore, we report the hydrodynamic parameters obtained for the isotropic model. Model selection for each residue was determined using the protocol of Mandel et al. (*33*). Four residues, S20, E23, K26, and F90, could not be fitted to any model. Extracted model-free parameters are presented in Supporting Information Table 2.

The analysis of the R_1, R_2, and $^1H-^{15}N$ NOE values provides information on the internal motion of the backbone amide on both a fast (ps−ns) and slow (μs−ms) time scale. The generalized order parameter (S^2) measures the amplitude of the internal motion on the fast time scale. The S^2 value plotted against the residue number is shown in Figure 2A. The average value of S_{avg}^2 over all residues is 0.71 ± 0.26. The general order parameter (S^2) values are quite uniform across individual helices: the average S_{avg}^2 values for residues in helices 1−4 are 0.89 ± 0.06, 0.84 ± 0.04, 0.77 ± 0.08, and 0.91 ± 0.04, respectively. The highest order parameters ($S^2 \sim 0.9$) are clustered primarily in the first and fourth helices, which form the dimer interface, and to a lesser extent in helix 2 and 3, whereas S^2 values substantially below average tend to cluster in the calcium-binding sites, in the hinge region, and near the N- and C-termini. The relatively high flexibility of helix 3 is intriguing, given that helix 3 is known to reorient substantially with the addition of calcium in homologous S100 family members (*12, 13*).

Calcium-binding sites 12 and 34 show similar mean S^2 values (S_{avg}^2 values of 0.65 ± 0.25 and 0.69 ± 0.32, respectively), indicating somewhat less stability in the calcium-binding sites than in the helices. The large variation of these S_{avg}^2 values reflects the presence of high flexibility in the N-terminal part (12N, residues S20−K27, and 34N, residues D63−D67) and low flexibility in the C-terminal part (12C, residues F28−E33, and 34C, residues E69−E74) of each site. In fact, the C-terminal parts of these sites each contain the N-terminal part of the following helix (helix 2

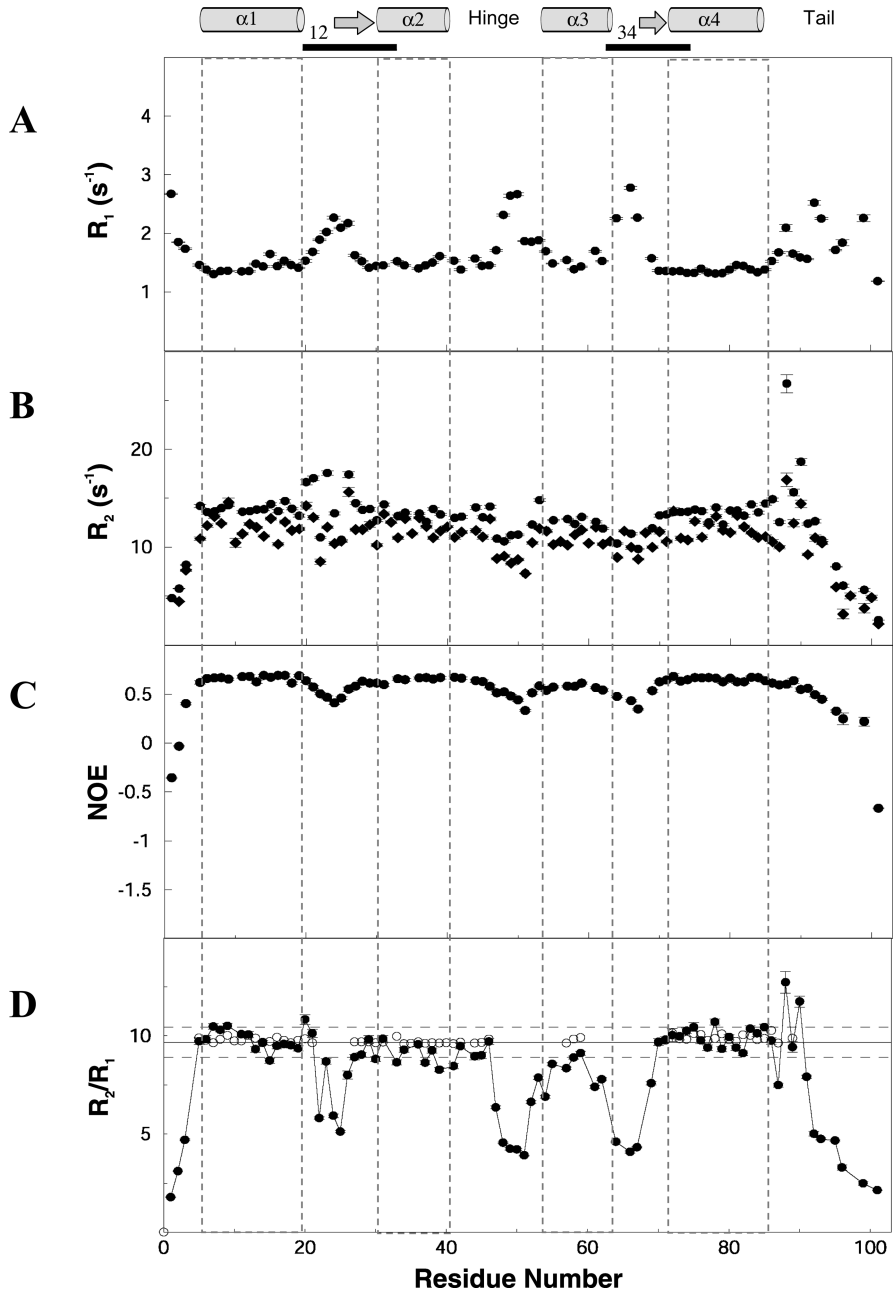

FIGURE 1: (A) R_1, (B) R_2, (C) $^{15}N-^{1}H$ heteronuclear NOE, and (D) the ratio R_2/R_1 for apo-Mts1, plotted vs residue number. All plots represent data collected at 600 MHz except filled diamonds are R_2 values at 500 MHz and open circles are calculated R_2/R_1 values using the program HYDRONMR. The solid line in the R_2/R_1 plot denotes $\langle R_2/R_1 \rangle$ of the core residues, and the dotted lines denote the $\pm 1.5\sigma$ $\langle R_2/R_1 \rangle$ positions. α helices 1−4 (amino acids 5−19, 31−40, 54−63, 72−85), calcium-binding sites 12 and 34 (20−33, 63−74), the hinge (41−53), and the C-terminal tail (86−101) are indicated above (A), along with short β strand regions present just N-terminal to helix 2 and helix 4.

and helix 4), preceded by a short stretch of β-strand (see secondary structure diagram above Figure 3A). These two strands hydrogen bond to each other within each monomer unit. The S^2_{avg} values are 0.44 ± 0.20, 0.29 ± 0.18, 0.85 ± 0.04, and 0.89 ± 0.08 for regions 12N, 34N, 12C, and 34C, respectively. Regions 12N and 34N also show large contributions from R_{ex}, indicating significant conformational exchange on the ms−μs time scale.

The hinge between the two EF-hands has a mean S^2_{avg} value similar to the calcium-binding loops (0.63 ± 0.22) and can also be divided into two distinct regions. Residues E41−L46 (HN) are more rigid ($S^2_{avg} = 0.85 \pm 0.05$) whereas residues G47−D53 (HC) are more flexible ($S^2_{avg} = 0.45 \pm 0.12$) and show significant conformational exchange contribution. The extreme N- and C-termini of Mts1 are highly flexible. The N-terminus (first 3 residues) has a mean S^2_{avg} value of 0.27 ± 0.26 and the C-terminal tail (last 16 residues) has a mean S^2_{avg} of 0.42 ± 0.25.

Figure 2B shows a ribbon plot of apo-Mts1 with residues colored according to S^2 value. Helices 1, 1′, 4, and 4′ are largely blue ($S^2 > 0.9$), forming a highly rigid four-helix hydrophobic core. Helices 2, 2′, 3, and 3′ are peripherally located and are mostly colored violet ($0.75 < S^2 < 0.9$) except the N-termini of helices 3 and 3′. However, points of contact between the central and peripheral helices often show similar order, suggesting that core−periphery contacts may influence internal mobility. The N-terminus of each calcium-binding site (12N and 34N) shows significant

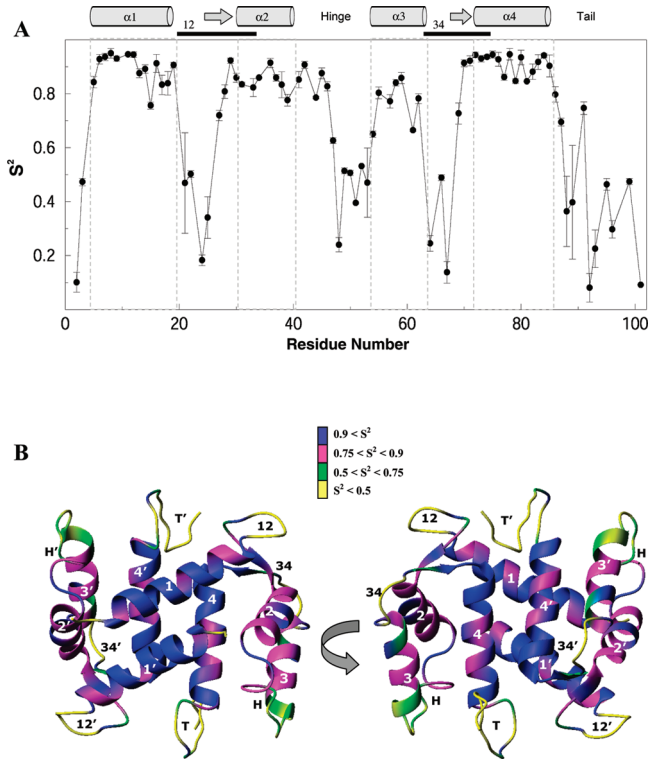

FIGURE 2: (A) Plot showing generalized order parameter (S^2) for apo-Mts1 vs residue number. (B) S^2 values painted on the ribbon plot of the apo-Mts1 structure (*47*).

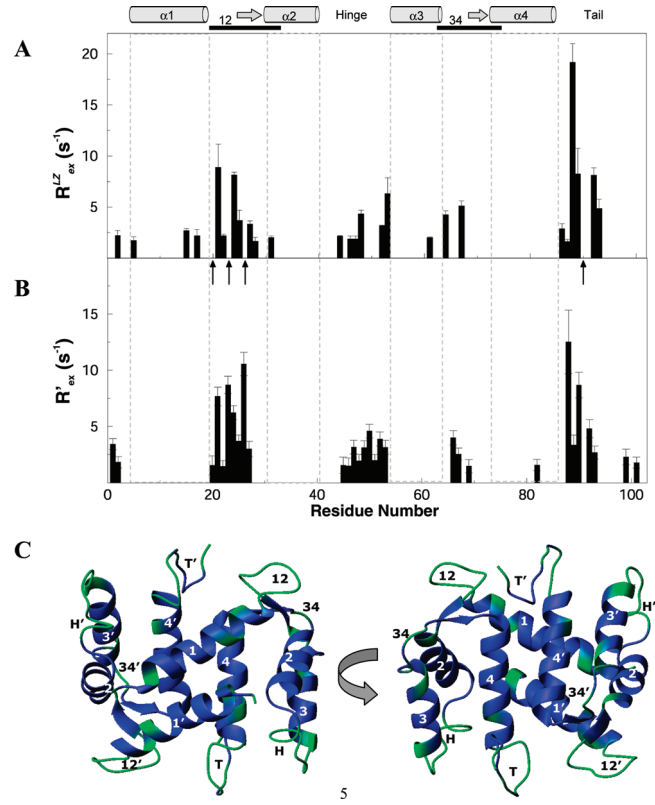

FIGURE 3: Residues with significant R_{ex} (>1.5 s^{-1}) indicated via (A) Lipari−Szabo model-free analysis (R_{ex}^{LZ}) and (B) cross-correlation relaxation rates of ^{15}N CSA and $^{15}N-^{1}H$ diplor interactions (R'_{ex}). (C) Residues with R_{ex}^{LZ} and R'_{ex} each above 1.5 s^{-1} are painted green on a ribbon plot of the apo-Mts1 NMR structure (*47*). The four vertical black arrows below (A) indicate residues for which relaxation data could be obtained but could not be fitted in model-free analysis.

flexibility (yellow in Figure 2B). The C-terminal tail and the hinge, which are relatively close together in space, each contain residues with a high degree of flexibility, suggesting the possible formation of a contiguous and yet dynamic surface for interaction with target proteins.

Fast internal motion relative to the overall correlation time is measured by the general order parameter, whereas large chemical-exchange contribution (R_{ex}) identifies residues that have conformational change in the slow time scale of μs to ms. Several important biochemical events such as protein−protein interactions, ligand or effector binding, enzymatic reactions, and dissociation rates often occur at slow time scales (μs−ms) (*17, 18, 40–42*). These slow processes can be measured indirectly by fitting relaxation data to Lipari−Szabo formalism or directly determined by comparison of transverse relaxation rates and cross-correlation rates (η_{xy}) between the ^{15}N CSA and $^{1}H-^{15}N$ dipolar relaxation (*24*). After fitting the relaxation data to Lipari−Szabo formalism, 24 residues showed indirect evidence of significant R_{ex}^{LZ} (>1.5 s^{-1}) as shown in Figure 3A. An additional four residues (S20, E23, K26, and F90, indicated by vertical arrows beneath Figure 3A) could not be fitted, and each has low NOE and high R_2 values relative to the rigid regions of the molecule, suggesting a high degree of dynamics, at least some of which is on a slow time scale. Direct measurement identified 30 residues with conformational exchange (R'_{ex} > 1.5 s^{-1}) on the μs−ms time scale (Figure 3B). Note that 19 residues showed significant R_{ex} in both analyses (compare panels A and B of Figure 3) and moreover that the R_{ex} terms group to the same regions of Mts1 via the two methods. Motions specifically on the 1−10 ms time scale were additionally probed using the relaxation compensated CPMG experiments, with τ_{CP} = 1 and 10 ms. However, no significant differences in relaxation rates were observed for these two experiments, suggesting that most of the observed dynamics lies outside of the low ms time scale.

There are clearly four distinct regions in Mts1 that show significant slow motion: the N-terminal regions of each calcium-binding site (12N and 34N), the C-terminal part of the hinge (HC) between α helices 2 and 3, and the N-terminal part of the C-terminal tail. These residues are colored green in the ribbon plot of the apo-Mts1 structure in Figure 3C. Interestingly, these regions are significantly more dynamic than the analogous regions of apo-S100B (*37*) and apocalbindin D_{9k} (*43*), the other two members of the S100 family for which ^{15}N relaxation studies have been published. Residues from the dimerization interface helices (1 and 4) do not show significant slow motions with the exception of T15 and H17 from helix 1 and I82 from helix 4, none of which was detected in both the model-free and cross-correlation schemes. Note that these three residues are not directly involved in the dimer interface. However, it is interesting to note that residue H17 of Mts1, which is solvent exposed, corresponds to S100B residue H15, which also shows slow motion (*37*) and is believed to interact with the nearby C-terminal tail. Similarly, residue I82 of Mts1 corresponds to V80 of S100B, which also shows slow motion (*37*) and is part of the hydrophobic surface that interacts with p53 (*9*). The lack of significant R_{ex} elsewhere in helices 1 and 4, along with high S^2, suggests that negligible conformational exchange between the monomer and dimer is

present and that the dimer interface of Mts1 is rigid on the time scales of this study (ms−ps).

It is instructive to discuss the binding events that may be associated with the R_{ex} terms in these four regions. Clearly, the calcium-binding site 12 and 34 R_{ex} terms may be associated with the readiness for binding calcium. Previously, we showed that, during calcium titration, site 12 fills earlier than site 34 (*20*). This filling order is unique to Mts1 as in all other S100 family proteins studied to date, site 34 has higher affinity toward calcium while site 12 subsequently fills in a highly cooperative manner. The current relaxation study shows that site 12 contains a large number of residues (S20−K28 and K31) with significant slow motion, but only a few residues from site 34 (S64, R66, D67, and E69) exhibit slow motion. Three residues from site 34 (D63, N65, and N68) could not be analyzed due to spectral overlap. However, for residues that could be measured, there is also a substantial difference is the magnitude of the R_{ex} values for these two sites (mean measured R'_{ex} values of site 12 and site 34 are 5.36 and 2.7, respectively). This could help to explain the earlier filling of site 12 in Mts1 upon calcium binding, as slow dynamics is often associated with a region primed for interaction with a ligand (*17, 18*).

The hinge region and C-terminal tail are also prime candidates for interactions with other proteins, based upon their R_{ex} terms. Furthermore, these two regions change conformation upon addition of calcium: helix 4 extends into the tail region simultaneously with the filling of site 12, whereas the hinge region shows somewhat decreased helical character simultaneously with the subsequent filling of site 34 (*20*). Extension of helix 4 upon calcium binding and/or addition of target ligand have also been reported in other S100 family proteins, e.g., see refs *9* and *44*. It was suggested that the distinct filling order in association with coordinated changes in the tail and hinge may provide an opportunity to determine the important regions for binding to specific target proteins (*20*). It has since been shown that in the case of MHC-IIA, which interacts with calcium-bound Mts1, a mutation that abolishes the ability of site 12 to bind calcium does not affect binding to MHC-IIA, whereas a similar mutation to site 34 does (*8*). Subsequently, this fact was independently confirmed, and it was further shown that the C-terminal tail is necessary for this interaction (*45*), all of which is consistent with the filling order and coordinated changes in the tail and hinge discussed above. The present study shows that slow dynamics is present in the C-terminal tail in the absence of calcium. The fact that the tail is important for binding MHC-IIA in the presence of calcium suggests that some of this slow dynamics may survive after calcium binding, but direct confirmation of this fact requires a relaxation study of the calcium-bound form of Mts1.

It has also been shown that in migrating breast cancer-derived cell lines, Mts1 colocalizes with MHC-IIA at the leading edge of lamellipodia (*8*). Interestingly, a double mutant with disrupted calcium binding to both site 12 and site 34 of Mts1 nonetheless retains this colocalization ability. As this mutant cannot produce the calcium-induced changes to the hinge and tail region thought to be necessary for interaction with MHC-II, these results suggest the presence of another binding partner for Mts1 which does not require calcium and in fact may specifically bind to the apo form of Mts1. In this regard, the slow dynamics present in the apo-

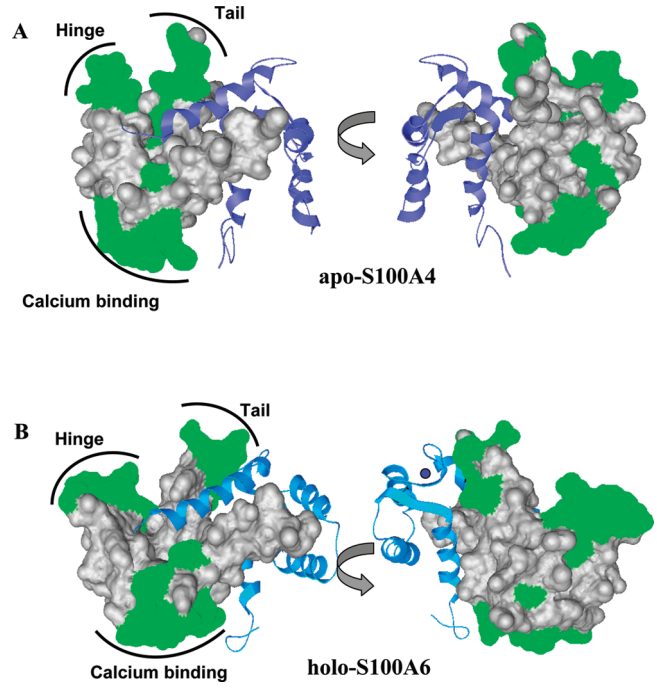

FIGURE 4: Surface plot of residues with confirmed intermediate conformational exchange (R_{ex}), as defined in Figure 3C. In each case, one momoner unit of the dimer pair is shown as a surface plot with exchanging regions painted green, while the other monomer is shown as a blue backbone ribbon diagram. (A) Apo-Mts1 (*47*). (B) Holo-S100A6 (*13*).

Mts1 hinge and tail regions, along with site 12 and site 34, could play a role. Figure 4A shows that these surfaces form a nearly contiguous surface (in green) covering the top and the bottom of the dimer in this view. It should be noted however that, in the context of biosensor assays, MHC-IIA interacts with Mts1 and p53, but not actin, tropomyosin, or tubulin, in the presence and absence of calcium (*46*). This combined with the above results leads to the suggestion that binding to the biosensor surface may induce the Mts1 structure to mimic in some way the calcium-bound form (*46*). This further raises the question as to whether other calcium-independent interactions could induce similar changes in Mts1 and thus whether Mts1 may indeed interact with MHC-IIA in the leading edge of lamellipodia in the absence of calcium due to changes induced by other binding partners.

Homology modeling starting with a variety of S100 proteins as a basis suggested that the holo-Mts1 conformation may closely resemble that of holo-S100A6 (*47*). Figure 4B shows a surface plot of the holo-S100A6 (pdb accession 1A03) with the residues homologous to the Mts1 residues undergoing R_{ex} painted in green. In this holo-form model, the hinge and the C-terminal tail are no longer contiguous. Rather, they would appear to form the edges of a pocket which may serve to grasp binding partners. Once again, it is likely that at least some slow dynamics remains in these regions in the holo form, but further experiments are necessary for confirmation.

Comparison with Other S100 Proteins. Two members of the S100 family, S100B (*37*) and calbindin D_{9k} (*43*), have been examined via NMR relaxation analysis. Calbindin D_{9k} is atypical of the S100 family as it does not dimerize in solution, does not undergo significant structural rearrangement upon calcium binding, and has no known binding partner and the C-terminus is shorter than Mts1 by 17

```
                    10          20          30          40
Mts1    MARP*LEEALD VIVSTFHKY*S GKEGDKFKLN *KTELKELLTR* KLPSFLGKRT
S100B   --S*ELEKAMV ALIDVFHQYS* GREGDKHKLK *KSELKELINN E*LSHFLEEIK
calbin  ---SAKKS*PE ELKGIFEKYA* AKEGDPNQLS *KEELKLLLQT E*FPSLLKGPS
                            b   b b  b w  ‡

                    60          70          80          90
Mts1    DEA*AFQKVMS NLD*SNRDNEV D*FQEYCVFLS CIAMM*CNEFF EGCPDKEPRK K
S100B   E*QEVVDKVME TL*DEDGDGEC D*FQEFMAFVS MVTTA*CHEFF EHE
calbin  T---*LDELFE EL*DKNGDGEV S*FEEF*QVLVK K*ISQ
                          s s s b  w  ‡
```

FIGURE 5: Sequence alignment of Mts1 with S100B and calbindin D_{9k}. Residues in helices 1, 2, 3, and 4 of the apo form of each protein are shown in bold italic. Calcium-binding sites 12 and 34 are underlined, with specific residues that coordinate calcium via the backbone carbonyl oxygen (b), a single side chain oxygen (s), and two side chain oxygens (‡) or via a bridging water (w) indicated beneath the underline.

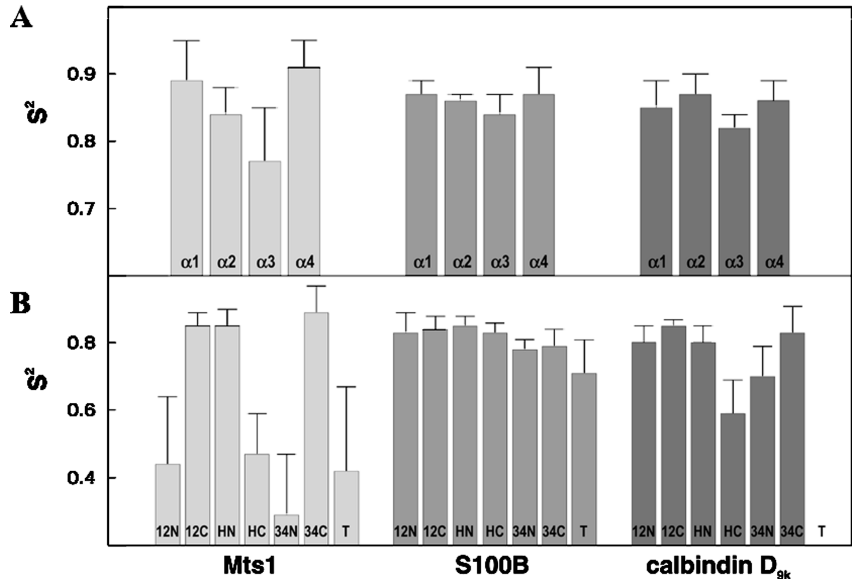

FIGURE 6: Comparison of the mean generalized order parameter S^2_{avg} across the indicated homologous regions of apo-Mts1 (current study), S100B (*37*), and calbindin D_{9k} (*43*). (A) Each of the four helices, labeled α1 through α4. (B) The N- and C-terminal sections of each calcium-binding site and the hinge regions corresponding to the following residues in Mts1: 12N, S20−K26; 12C, F27−E33, HN, E41−L46; HC, G47−D53; 34N, D63−N68; 34C, E69−E74. The C-terminal tail (T) region is also shown. The error bars indicate the standard deviation of the S^2 values across the given region.

residues (Figure 5). In addition, the calbindin N-terminus contains three fewer residues than Mts1, and helices 1, 3, and 4 are each shortened relative to Mts1 and S100B. S100B, like Mts1, exists as a dimer in solution, demonstrates significant rearrangement upon addition of calcium, binds several target proteins including p53 (*9*), and contains two fewer N-terminal and eight fewer C-terminal residues than Mts1 (Figure 5).

The global correlation time (τ_c) extracted for the 24.2 kDa dimeric Mts1 (106 residues per monomer, including a 5-residue N-terminal cloning artifact) is 9.94 ± 0.06 ns at 40 °C, with a similar value determined via HYDRONMR. The reported τ_c for the 21.4 kDa dimeric S100B (91 residues) is 7.80 ± 0.03 ns at 37 °C, which corresponds to 7.29 ns at 40 °C (*37*). This difference may be related in part to the different lengths of the C-terminal tail and the related ~13% increase in the molecular mass or to differences in dynamics as discussed below. As a point of reference, a global correlation time of 7.6 ns at 32 °C was reported in the absence of calcium for α-parvalbumin, a non-S100 family monomeric 12 kDa EF-hand protein with a similar $D_{\parallel}/D_{\perp}$ ratio as Mts1 (*48*). Calbindin D_{9k} is monomeric and as expected has a shorter global correlation time, $\tau_c = 4.25 \pm 0.01$ ns at 27 °C (*49*). When scaled for molecular mass, temperature, and viscosity, the α-parvalbumin and calbindin D_{9k} correlation times correspond to approximately 12 and 8 ns, respectively, for a protein the size of Mts1 at 40 °C.

Figure 6A shows a comparison of average order parameter (S^2_{avg}) values for each helix in these three proteins. The error bars indicate the standard deviation across the residues of the helix, rather than the experimental uncertainty. The Mts1 and S100B (*37*) helices show a similar pattern, with a highest levels of rigidity in the dimer interface helices 1 and 4 and the highest level of dynamics in helix 3. However, this pattern is more pronounced, and the standard deviations are larger in the case of Mts1. Calbindin D_{9k}, on the other hand, has highest S^2_{avg} in the second helix (*43*), essentially with helix 1 and 2 swapping places in the degree of order hierarchy. These combined facts would seem to suggest that dimerization of Mts1 and S100B may be a factor in the high stability of helices 1 and 4. Furthermore, the lack of any significant conformational exchange (R_{ex}) and good agreement between the calculated (HYDRONMR) and experimental hydrodynamics parameters (Figure 1, bottom panel) for the residues in helix 1 and 4 clearly suggest that Mts1 is overwhelmingly in one oligomeric state, the dimer. Interestingly, while all three proteins have lowest S^2_{avg} values in helix 3, the Mts1 helix 3 is significantly more flexible than in

S100B or calbindin D_{9k}. The third helix in S100 proteins is generally known to reorganize upon calcium binding (*50*). In Mts1, the C-terminal region of the hinge and the N-terminal region of the helix 3 show more flexibility than in the other two proteins. Interestingly, the position of helix 3 relative to helix 4 also shows variability, with the helix 3 position in Mts1 most closely resembling that found in S100A6 (*47*). It was suggested that this difference in the position of helix 3 may be due to differences in the amino acid sequence in the C-terminus of helix 4 and the hinge region (HC). In S100B, three residues, one each from the hinge region (I47, S^2 not fit), the N-terminal region of helix 3 (V52, $S^2 = 0.85$), and the C-terminal region of helix 4 (A83, $S^2 = 0.87$), form a hydrophobic core that helps to stabilize the position of helix 3. However, in Mts1, the homologous residues (R49, $S^2 = 0.51$; A54, $S^2 = 0.65$; M85, $S^2 = 0.90$) are significantly less hydrophobic and more flexible at the A54 and R49 positions, and R49 in addition shows significant slow motion in μs−ms time scale. Thus, these three residues may not interact in a sufficient manner to stabilize the position of helix 3. Calbindin D_{9K}, however, does not dimerize and does not reorganize significantly with addition of calcium (*49*), yet this protein also appears to have somewhat greater flexibility in helix 3 than in the other helices. Further comparative relaxation studies of S100 proteins will be necessary to draw conclusions regarding a possible correlation between internal motion, the reorientation of helices upon addition of calcium, and increased stability at the dimer interface.

Figure 6B shows a comparison of S^2_{avg} values for the calcium-binding sites 12 and 34, the intervening hinge, and the C-terminal tail. The calcium-binding sites are further subdivided on the basis of Mts1 S^2 values (see Figure 2A) into N-terminal flexible regions (12N, $S^2_{avg} = 0.44$; 34N, $S^2_{avg} = 0.29$) and C-terminal rigid regions (12C, $S^2_{avg} = 0.85$; 34C, $S^2_{avg} = 0.90$). The hinge regions are similarly divided, though in this the N-terminal hinge residues are more rigid than the C-terminal hinge (HN, $S^2_{avg} = 0.85$; HC, $S^2_{avg} = 0.47$). Looking first at the calcium-binding sites, each of the three proteins have similar, fairly high S^2_{avg} values for the 12C and 34C regions. However, S100B and calbindin D_{9k} show only a slight indication of the increased flexibility in the 12N and 34N regions which are highly flexible in Mts1. Each of the three proteins also requires R_{ex} terms in model-free analysis for fitting both the 12 and 34 regions, though to varying extents: Mts1, S100B, and calbindin D_{9K}, respectively, require R_{ex} terms to fit 11, 5, and 8 residues from sites 12 and 34 combined. In each case, site 12 requires more R_{ex} terms than site 34, and the N-terminal region of each site requires more R_{ex} terms than the C-terminal region. The number of residues with $R_{ex} > 1.5\ s^{-1}$ reduces to 9, 2, and 1, respectively, for the three proteins, suggesting that a higher degree of μs−ms time scale motion may be present for Mts1. Note that cross-correlation experiments (Figure 3B) provide direct confirmation of R_{ex} in the case of Mts1 and also implicate additional residues not counted in the above totals.

This marked increase in flexibility of the Mts1 calcium-binding regions relative to S100B and calbindin D_{9k} may be related to the atypical calcium-filling properties of Mts1: among S100 proteins investigated, only Mts1 fills site 12 prior to site 34 during calcium titration. If we assume that higher affinity is related to a higher flexibility, then the filling of site 34 prior to site 12 in S100B and calbindin D_{9k} is consistent with the slightly lower order parameters in site 34 (Figure 6B) but is inconsistent with the higher degree of R_{ex} in site 12 for these two proteins. Conversely, the earlier filling of Mts1 site 12 is consistent with the increased R_{ex} in site 12. The average order parameters of sites 12 and 34 for Mts1 are similar.

Although the three-dimensional structures of the S100 family proteins are quite similar, they bind to distinct sets of proteins. This specificity is generally attributed to the low similarity regions of the hinge and C-terminal tail. A comparison of relaxation data shows that these regions also vary significantly in dynamic properties from protein to protein. Each of the three proteins has similar fairly high S^2 values in the N-terminal half of the hinge (HN in Figure 6B). However, Mts1 and calbindin D_{9k}, but not S100B, have reduced order parameters in the HC region. Many residues in the Mts1 hinge region exhibit significant slow motion (Figure 3) compared to only three residues for S100B and none for calbindin D_{9k}. Interestingly, in S100B, the three hinge residues showing slow motion are I47, which forms part of the hydrophobic triad stabilizing the position of helix 3 as discussed above, and the flanking residues E46 and K48. Similarly, the C-terminal tail of Mts1 is more flexible ($S^2_{avg} = 0.42$) than the shorter tail of S100B ($S^2_{avg} = 0.71$) (Figure 6B), while calbindin D_{9k} has no tail. In S100B, the tail (C84−E91) together with the C-terminus of helix 4 (T81−A83) shows severe exchange broadening, suggesting significant slow dynamic events involving the S100B C-terminal 11 residues. Interestingly, upon binding p53 but not upon binding calcium, the S100B helix 4 extends by five residues with a concomitant loss of conformational exchange for these residues (*9*). In Mts1, a similar lengthening of helix 4 is seen upon addition of calcium (*20*). The current study shows that most of the residues involved in this extension show slow motion in the μs−ms time scale.

Vallely and co-workers (*47*) proposed a subclassification of S100 proteins into two families based in part on the identity of the residue corresponding to amino acid numbers 49 and 85 in Mts1. In this scheme, Mts1, along with S100A2, -A3, and -A6, comprises subfamily 1, while most other S100 proteins fall into subfamily 2. Calbindin D_{9k}, an atypical S100 protein, lies outside of this classification scheme. The present study indicates that residue 49 in Mts1 is more mobile than its counterpart in S100B. This result could suggest that other subfamily 1 S100 proteins may be more flexible than their subfamily 2 counterparts.

CONCLUSIONS

Analysis of relaxation parameters indicates that Mts1 has a highly structured and rigid core consisting of helices 1 and 4 of each monomer, which combine to form the dimer interface. This rigid core is flanked by helices 2 and 3, which show somewhat lower S^2_{avg} values. The structured regions of the two EF-hand calcium-binding sites have similar S^2_{avg} values, but the N-terminal regions of each site (12N and 34N) are more flexible and further exhibit slow motion in the μs−ms time scales. The number of residues with detected R_{ex} values from model-free analysis, largely confirmed by cross-correlation studies, is higher for the 12N than for the 34N region, which may help to explain the preferential filling

of site 12 by calcium. The hinge in Mts1 also contains two distinct regions. In this case, the N-terminal region (HN) shows less internal motion than the C-terminal part of the hinge (HC). The less flexible HN region shows a similar degree of order as the analogous N-terminal region of the S100B and calbindin D_{9k} hinge. The long flexible tail of Mts1 is likely a key factor in causing Mts1 to tumble more slowly than S100B, although added flexibility in the C-terminal portion of the hinge (HC) and the N-terminal half of each calcium-binding site may also play a role. The flexible HC region of Mts1 resembles the dynamic calbindin D_{9K} HC region, which has greater mobility than the calbindin calcium-binding loops. Mts1 has a long flexible C-terminal tail (low S^2_{avg}), the N-terminal part of which becomes helical to extend helix 4 upon addition of calcium. These extending residues also show significant R_{ex} behavior in the absence of calcium. The flexible parts of the hinge and tail form a nearly contiguous surface with R_{ex} behavior that may be attractive to prospective ligands. This surface is further contiguous to calcium-binding sites 12 and 34 from the partner monomer unit, which also display R_{ex} behavior. It seems plausible then that unknown binding partners of apo-Mts1 may contact the hinge, tail, and possibly even the 12 and 34 regions, though clearly the primary function of the 12 and 34 regions is to bind calcium and tight binding of a partner to these regions would prevent calcium coordination. It also seems plausible that calcium coordination to sites 12 and 34 may alter the dynamics of the hinge and tail. Further studies will be necessary to determine whether, in calcium-loaded Mts1, some degree of slow dynamics remains in these regions and whether this flexibility plays a role in calcium-dependent interactions of Mts1 with target proteins.

SUPPORTING INFORMATION AVAILABLE

Table 1 listing R_1, R_2, and NOE values and their uncertainties and Table 2 providing extracted model-free parameters from Lipari−Szabo analysis. This material is available free of charge via the Internet at http://pubs.acs.org.

REFERENCES

1. Ebralidze, A., Tulchinsky, E., Grigorian, M., Afanasyeva, A., Senin, V., Revazova, E., and Lukanidin, E. (1989) Isolation and characterization of a gene specifically expressed in different metastatic cells and whose deduced gene product has a high degree of homology to a Ca^{2+}-binding protein family. *Genes Dev. 3*, 1086–1093.
2. Grigorian, M., Tulchinsky, E., Burrone, O., Tarabykina, S., Georgiev, G., and Lukanidin, E. (1994) Modulation of mts1 expression in mouse and human normal and tumor cells. *Electrophoresis 15*, 463–468.
3. Maelandsmo, G. M., Hovig, E., Skrede, M., Engebraaten, O., Florenes, V. A., Myklebost, O., Grigorian, M., Lukanidin, E., Scanlon, K. J., and Fodstad, O. (1996) Reversal of the in vivo metastatic phenotype of human tumor cells by an anti-CAPL (mts1) ribozyme. *Cancer Res. 56*, 5490–5498.
4. Grigorian, M., Ambartsumian, N., Lykkesfeldt, A. E., Bastholm, L., Elling, F., Georgiev, G., and Lukanidin, E. (1996) Effect of mts1 (S100A4) expression on the progression of human breast cancer cells. *Int. J. Cancer 67*, 831–841.
5. Rosenblum, J. S., and Barbas, C. F. I. (1995) Synthetic antibodies, in *Antobody Engineering* (Borrenbaeck, C. A. K., Ed.) 2nd ed., pp 89−116, Oxford University Press, Oxford.
6. Novitskaya, V., Grigorian, M., Kriajevska, M., Tarabykina, S., Bronstein, I., Berezin, V., Bock, E., and Lukanidin, E. (2000) Oligomeric forms of the metastasis-related Mts1 (S100A4) protein stimulate neuronal differentiation in cultures of rat hippocampal neurons. *J. Biol. Chem. 275*, 41278–41286.
7. Ambartsumian, N., Klingelhofer, J., Grigorian, M., Christensen, C., Kriajevska, M., Tulchinsky, E., Georgiev, G., Berezin, V., Bock, E., Rygaard, J., Cao, R. H., Cao, Y. H., and Lukanidin, E. (2001) The metastasis-associated Mts1(S100A4) protein could act as an angiogenic factor. *Oncogene 20*, 4685–4695.
8. Kim, E. J., and Helfman, D. M. (2003) Characterization of the metastasis-associated protein, S100A4. Roles of calcium binding and dimerization in cellular localization and interaction with myosin. *J. Biol. Chem. 278*, 30063–30073.
9. Rustandi, R. R., Baldisseri, D. M., and Weber, D. J. (2000) Structure of the negative regulatory domain of p53 bound to S100B(betabeta). *Nat. Struct. Biol. 7*, 570–574.
10. Lewit-Bentley, A., Rety, S., Sopkova-de Oliveira Santos, J., and Gerke, V. (2000) S100-annexin complexes: Some insights from structural studies. *Cell Biol. Int. 24*, 799–802.
11. Rety, S., Sopkova, J., Renouard, M., Osterloh, D., Gerke, V., Tabaries, S., Russo-Marie, F., and Lewit-Bentley, A. (1999) The crystal structure of a complex of p11 with the annexin II N-terminal peptide. *Nat. Struct. Biol. 6*, 89–95.
12. Drohat, A. C., Baldisseri, D. M., Rustandi, R. R., and Weber, D. J. (1998) Solution structure of calcium-bound rat S100B(betabeta) as determined by nuclear magnetic resonance spectroscopy. *Biochemistry 37*, 2729–2740.
13. Otterbein, L. R., Kordowska, J., Witte-Hoffmann, C., Wang, C. L. A., and Dominguez, R. (2002) Crystal structures of S100A6 in the Ca^{2+}-free and Ca^{2+}-bound states: The calcium sensor mechanism of S100 proteins revealed at atomic resolution. *Structure 10*, 557–567.
14. Skelton, N. J., Kordel, J., and Chazin, W. J. (1995) Determination of the solution structure of apo calbindin D9k by NMR spectroscopy. *J. Mol. Biol. 249*, 441–462.
15. Teigelkamp, S., Bhardwaj, R. S., Roth, J., Meinardushager, G., Karas, M., and Sorg, C. (1991) Calcium-dependent complex assembly of the myeloic differentiation proteins Mrp-8 and Mrp-14. *J. Biol. Chem. 266*, 13462–13467.
16. Donato, R. (1999) Functional roles of S100 proteins, calcium-binding proteins of the EF-hand type. *Biochim. Biophys. Acta 1450*, 191–231.
17. Ishima, R., and Torchia, D. A. (2000) Protein dynamics from NMR. *Nat. Struct. Biol. 7*, 740–743.
18. Mittermaier, A., and Kay, L. E. (2006) New tools provide new insights in NMR studies of protein dynamics. *Science (New York) 312*, 224–228.
19. Henzler-Wildman, K. A., Lei, M., Thai, V., Kerns, S. J., Karplus, M., and Kern, D. (2007) A hierarchy of timescales in protein dynamics is linked to enzyme catalysis. *Nature 450*, 913–916.
20. Dutta, K., Cox, C. J., Huang, H., Basavappa, R., and Pascal, S. M. (2002) Calcium coordination studies of the metastatic Mts1 protein. *Biochemistry 41*, 4239–4245.
21. Sun, X., Zhang, Q., and Al-Hashimi, H. M. (2007) Resolving fast and slow motions in the internal loop containing stem-loop 1 of HIV-1 that are modulated by Mg^{2+} binding: role in the kissing-duplex structural transition. *Nucleic Acids Res. 35*, 1698–1713.
22. Alexandrov, A., Dutta, K., and Pascal, S. M. (2001) MBP-fusion with a viral protease cleavage site: one-step cleavage/purification of insoluble proteins. *BioTechniques 30*, 1194–1198.
23. Loria, J. P., Rance, M., and Palmer, A. G., III. (1999) A relaxation-compensated Carr-Purcell-Meiboom-Gill sequence for characterizing chemical exchange by NMR spectroscopy. *J. Am. Chem. Soc. 121*, 2331–2332.
24. Kroenke, C. D., Loria, J. P., Lee, L. K., Rance, M., and Palmer, A. G. (1998) Longitudinal and transverse H-1-N-15 dipolar N-15 chemical shift anisotropy relaxation interference: Unambiguous determination of rotational diffusion tensors and chemical exchange effects in biological macromolecules. *J. Am. Chem. Soc. 120*, 7905–7915.
25. Fushman, D., Tjandra, N., and Cowburn, D. (1998) Direct measurement of N-15 chemical shift anisotropy in solution. *J. Am. Chem. Soc. 120*, 10947–10952.
26. Wang, C. Y., Rance, M., and Palmer, A. G. (2003) Mapping chemical exchange in proteins with MW > 50 kD. *J. Am. Chem. Soc. 125*, 8968–8969.
27. Pelupessy, P., Espallargas, G. M., and Bodenhausen, G. (2003) Symmetrical reconversion: measuring cross-correlation rates with enhanced accuracy. *J. Magn. Reson. 161*, 258–264.
28. Johnson, B. A., and Blevins, R. A. (1994) NMRView: A computer program for the visualization and analysis of NMR data. *J. Biomol. NMR 4*, 603–614.

29. Farrow, N. A., Muhandiram, R., Singer, A. U., Pascal, S. M., Kay, C. M., Gish, G., Shoelson, S. E., Pawson, T., Forman-Kay, J. D., and Kay, L. E. (1994) Backbone dynamics of a free and phosphopeptide-complexed Src homology 2 domain studied by ^{15}N NMR relaxation. *Biochemistry 33*, 5984–6003.
30. Lipari, G., and Szabo, A. (1982) Model-free approach to the interpretation of nuclear magnetic resonance relaxation in macromolecules. 1. Theory and range of validity. *J. Am. Chem. Soc. 104*, 4546–4559.
31. Bax, A., Clore, G. M., Driscoll, P. C., Gronenborn, A. M., Ikura, M., and Kay, L. E. (1990) Practical aspects of proton-carbon-carbon-proton three-dimensional correlation spectroscopy of ^{13}C-labeled proteins. *J. Magn. Reson. 87*, 620–627.
32. Fushman, D., Cahill, S., and Cowburn, D. (1997) The main-chain dynamics of the dynamin pleckstrin homology (PH) domain in solution: Analysis of N-15 relaxation with monomer/dimer equilibration. *J. Mol. Biol. 266*, 173–194.
33. Mandel, A. M., Akke, M., and Palmer, A. G., III. (1995) Backbone dynamics of *Escherichia coli* ribonuclease HI: correlations with structure and function in an active enzyme. *J. Mol. Biol. 246*, 144–163.
34. de la Torre, J. G., Huertas, M. L., and Carrasco, B. (2000) HYDRONMR: Prediction of NMR relaxation of globular proteins from atomic-level structures and hydrodynamic calculations. *J. Magn. Reson. 147*, 138–146.
35. Tjandra, N., Feller, S. E., Pastor, R. W., and Bax, A. (1995) Rotational diffusion anisotropy of human ubiquitin from ^{15}N NMR relaxation. *J. Am. Chem. Soc. 117*, 12562–12566.
36. Dutta, K., Cox, C. J., Alexandrov, A., Huang, H., Basavappa, R., and Pascal, S. M. (2002) Sequence-specific chemical shift assignment and chemical shift indexing of murine apo-Mts1. *J. Biomol. NMR 22*, 181–182.
37. Inman, K. G., Baldisseri, D. M., Miller, K. E., and Weber, D. J. (2001) Backbone dynamics of the calcium-signaling protein apo-S100B as determined by ^{15}N NMR relaxation. *Biochemistry 40*, 3439–3448.
38. Lipari, G., and Szabo, A. (1982) Analysis of NMR relaxation data on macromolecules using the model-free approach. *Biophys. J. 37*, A380−A380.
39. Flynn, P. F., Bieber Urbauer, R. J., Zhang, H., Lee, A. L., and Wand, A. J. (2001) Main chain and side chain dynamics of a heme protein: ^{15}N and ^{2}H NMR relaxation studies of *R. capsulatus* ferrocytochrome c_2. *Biochemistry 40*, 6559–6569.
40. Epstein, D. M., Benkovic, S. J., and Wright, P. E. (1995) Dynamics of the dihydrofolate-reductase folate complex−Catalytic sites and regions known to undergo conformational change exhibit diverse dynamical features. *Biochemistry 34*, 11037–11048.
41. Dutta, K., Shi, H., Cruz-Chu, E. R., Kami, K., and Ghose, R. (2004) Dynamic influences on a high-affinity, high-specificity interaction involving the C-terminal SH3 domain of p67phox. *Biochemistry 43*, 8094–8106.
42. Kempf, J. G., Jung, J. Y., Ragain, C., Sampson, N. S., and Loria, J. P. (2007) Dynamic requirements for a functional protein hinge. *J. Mol. Biol. 368*, 131–149.
43. Akke, M., Skelton, N. J., Kordel, J., Palmer, A. G., and Chazin, W. J. (1993) Effects of ion-binding on the backbone dynamics of calbindin-D9k determined by N-15 NMR relaxation. *Biochemistry 32*, 9832–9844.
44. Rustandi, R. R., Drohat, A. C., Baldisseri, D. M., Wilder, P. T., and Weber, D. J. (1951) (1998) The Ca(2+)-dependent interaction of S100B(beta beta) with a peptide derived from p53. *Biochemistry 37*, 1960.
45. Zhang, S., Wang, G. Z., Liu, D., Bao, Z. Z., Fernig, D. G., Rudland, P. S., and Barraclough, R. (2005) The C-terminal region of S100A4 is important for its metastasis-inducing properties. *Oncogene 24*, 4401–4411.
46. Chen, H. L., Fernig, D. G., Rudland, P. S., Sparks, A., Wilkinson, M. C., and Barraclough, R. (2001) Binding to intracellular targets of the metastasis-inducing protein, S100A4 (p9Ka). *Biochem. Biophys. Res. Commun. 286*, 1212–1217.
47. Vallely, K. M., Rustandi, R. R., Ellis, K. C., Varlamova, O., Bresnick, A. R., and Weber, D. J. (2002) Solution structure of human Mts1 (S100A4) as determined by NMR spectroscopy. *Biochemistry 41*, 12670–12680.
48. Baldellon, C., Alattia, J. R., Strub, M. P., Pauls, T., Berchtold, M. W., Cave, A., and Padilla, A. (1998) N-15 NMR relaxation studies of calcium-loaded parvalbumin show tight dynamics compared to those of other EF-hand proteins. *Biochemistry 37*, 9964–9975.
49. Skelton, N. J., Palmer, A. G. I., Akke, M., Kördel, J., Rance, M., and Chazin, W. J. (1993) Proctical aspects of two-dimensional proton-detected ^{15}N spin relaxation measurements. *J. Magn. Reson. B 102*, 253–264.
50. Osterloh, D., Ivanenkov, V. V., and Gerke, V. (1998) Hydrophobic residues in the C-terminal region of S100A1 are essential for target protein binding but not for dimerization. *Cell Calcium 24*, 137–151.

BI8005048